https://doi.org/10.5194/se-2021-141
Preprint. Discussion started: 14 December 2021
© Author(s) 2021. CC BY 4.0 License.

Solid Earth Discussions

Postglacial strain rate - stress paradox, example of the Western Alps active faults

Juliette Grosset[1], Stéphane Mazzotti[1], and Philippe Vernant[1]
[1]Géosciences Montpellier, CNRS, Université de Montpellier, Montpellier, 34000, France
Correspondence: J. Grosset (juliette.grosset@umontpellier.fr)

Abstract. The understanding of the origins of seismicity in intraplate regions is crucial to better characterize seismic hazards. In formerly glaciated regions such as Fennoscandia North America or the Western Alps, stress perturbations from Glacial Isostatic Adjustment (GIA) have been proposed as a major cause of large earthquakes. In this study, we focus on the Western Alps case using numerical modeling of lithosphere response to the Last Glacial Maximum icecap. We show that the flexural response to GIA induces present-day stress perturbations of ca. 1-2 MPa, associated with horizontal extension rates up to ca. 2.5×10^{-9} yr^{-1}. The latter is in good agreement with extension rates of ca. 2×10^{-9} yr^{-1} derived from high-resolution geodetic (GNSS) data and with the overall seismicity deformation pattern. In the majority of simulations, stress perturbations induced by GIA promote fault reactivation in the internal massifs and in the foreland regions (i.e., positive Coulomb Failure Stress perturbation), but with predicted rakes systematically incompatible with those from earthquake focal mechanisms. Thus, although GIA explains a major part of the GNSS strain rates, it tends to inhibit the observed seismicity in the Western Alps. A direct corollary of this result is that, in cases of significant GIA effect, GNSS strain rate measurements cannot be directly integrated in seismic hazard computations, but instead require detailed modeling of the GIA transient impact.

1 Postglacial strain rate - stress paradox for intracontinental regions

The origins and characteristics of seismicity in Stable Continental Regions (SCR) are an ongoing conundrum in Earth science studies (e.g., Calais et al., 2016; Talwani, 2017). Because Plate Tectonics cannot be the main source of SCR seismicity, the transient stress perturbations of Glacial Isostatic Adjustment (GIA) are commonly considered to explain the recent seismic activity and fault surface ruptures following the Last Glacial Maximum in regions such as Fennoscandia or northern North America (e.g., Hetzel and Hampel, 2005; Steffen et al., 2014; Wu and Hasegawa, 1996). In these regions, the question of the forcing mechanism and its potential rapid decay on a time scale of 103–105 yr is a central issue for understanding the hazards posed by earthquakes up to magnitudes MW = 6–7.

The first-order mechanics associated with GIA-related seismicity involves loading/unloading flexure of the lithosphere, with associated stress perturbations up to a few MPa, sufficient to directly trigger earthquakes on near-failure-equilibrium fault (e.g., Johnston, 1987; Wu and Hasegawa, 1996) or to unclamp faults thus allowing the release of long-term stored tectonic stress (e.g., Craig et al., 2016). Both explanations (shear-stress increment over the failure threshold or normal-stress reduction) rely on the same model (Fig. 1), wherein the initial ice loading results in downward flexure associated with a horizontal compres-

https://doi.org/10.5194/se-2021-141
Preprint. Discussion started: 14 December 2021
© Author(s) 2021. CC BY 4.0 License.

sive stress perturbation in the upper half of the elastic lithosphere beneath the load (and upward flexure / extensive stress in the forebulge regions). Following the deglaciation, the lithosphere unbending is dampened by the mantle viscosity, resulting in a gradual diminution of the compressive stress perturbation. The associated strain corresponds to a maximum shortening at the glacial peak followed by a shortening diminution during the postglacial rebound phase. As a result, the present-day surface strain rate corresponds to an extension rate while the stress perturbation remains compressive. This apparent contradiction is similar to the strain rate - stress paradox observed in subduction zone forearcs in relation with transient interseismic locking of the megathrust fault (Wang, 2000).

Owing to the improvements in technology and time series durations, GNSS (Global Navigation Satellite Network) data allows measuring these small present-day extension rates coupled with vertical uplift rates in regions affected by postglacial rebound from the Last Glacial Maximum (e.g., Johansson et al., 2002; Tarayoun, 2018). Geodetic uplift rates have been classically used to constrain GIA models at global and regional scales (e.g., Mey et al., 2016; Peltier et al., 2015), whereas horizontal strain rates have been compared with seismicity deformation patterns and rates (Mazzotti et al., 2005; Rabin et al., 2018; Sue et al., 2007; Walpersdorf et al., 2018). One of the main goals of the latter comparison is the integration of GNSS velocities and strain rates in seismic hazard models, assuming that these short-term (5–20 yr) strain rates can provide information on long-term (10^4–10^5 yr) seismic fault activity. However, in regions of ongoing GIA, the conceptual model presented above and its apparent strain rate - stress paradox lead to strong doubts regarding the usability of GNSS strain rates for comparing with the seismicity. In the following, we test this question using elastic flexure models of the Western Alps to investigate the GIA effects on fault and seismic activity.

2 Western Alps: Seismicity and GNSS strain rates

The Western Alps is one of the most seismically active regions in western Europe (Fig. 2a), with several damaging instrumental and historical earthquakes (e.g. Epagny-Annecy, 1996, Mw = 5; Ligurian-Imperia, 1887, Mw = 6.8-6.9; Bale, 1356, Mw = 6.5 (Larroque et al., 2012; Meghraoui et al., 2001; Thouvenot et al., 1998)) and instrumental seismicity that covers the whole Alpine arc (Mw $\leq$ 5, Cara et al., 2015). Strain patterns derived from earthquake focal mechanisms show an overall extension direction perpendicular to the Alpine arc axis in the inner Alps, associated with strike-slip and arc-perpendicular shortening at the periphery in the foreland regions (Fig. 2b; Delacou et al., 2004; Mathey et al., 2021; Sue et al., 1999). A small part of these earthquakes are associated with known structures such as the Belledonne Fault (Thouvenot et al., 2003), the Durance Fault (Cushing et al., 2008) or the Vuache Fault (Rabin et al., 2018; Thouvenot et al., 1998). In contrast, most of the normal-faulting earthquakes in the internal massifs (above the Penninic Front) are not related to known structures (e.g., Sue et al., 2003).
The present-day Alpine tectonics are primarily controlled by the counter-clockwise rotation of the Adria microplate relative to Eurasia, with a rotation pole directly east of the Western Alps near Turin, northwestern Italy (Fig. 2a; Battaglia et al., 2004; D'Agostino et al., 2008). This kinematics is incompatible with the observed seismicity and geodetic horizontal deformation patterns (Fig. 2). In addition, GNSS data show a relative horizontal motion across the Western Alps below ca. 0.3 mm.yr^{-1}

https://doi.org/10.5194/se-2021-141
Preprint. Discussion started: 14 December 2021
© Author(s) 2021. CC BY 4.0 License.

(Masson et al., 2019), much slower than the vertical uplift rates that range between 0.5 and 2.5 mm.yr^{-1} in the inner Western Alps (e.g., Masson et al., 2019; Nocquet et al., 2016).

In details, the GNSS-derived horizontal strain rate field (Fig. 3) shows Alpine arc-perpendicular extension rates ca. 2×10^{-9} yr^{-1} in the inner regions (Switzerland, France-Italy border), associated with shortening rates ca. $1\breve{}2 \times 10^{-9}$ yr^{-1} in the foreland and surrounding areas from the Upper Rhine Graben to the Jura and Rhone Valley (Masson et al., 2019; Nguyen et al., 2016; Walpersdorf et al., 2018). The southern Western Alps are associated with a complex mix of extension and strike-slip rates ca. $1\breve{}2 \times 10^{-9}$ yr^{-1}. As shown by the original velocities (Fig. 3a), these signals are at the limit of GNSS detection and resolution and can only be extracted from the background noise using spatial filtering / smoothing technics. The results shown in Fig. 3 are based on a spatial Gaussian filtering with a half-width of 90 km (cf., Masson, 2019), which allows highlighting coherent strain rate signals at wavelength of ca. 150–200 km that we consider appropriate for comparison with ongoing GIA deformation due to the Alpine Icecap (cf. Fig. 3 and next section). Details of the Gaussian filtering method and additional strain rate maps at different filtering half-widths can be found in the Supplementary Material A2 to provide an overview of the strain rate patterns and their sensibility to the filtering wavelength.

This overall deformation pattern (slow horizontal extension / extension rates coupled with relatively fast uplift rates) is at the core of the current debate on the processes responsible for the ongoing Western Alps deformation. The role of plate tectonics being, at best, very small, alternative processes include mantle and slab-tear dynamics (Sternai et al., 2019), surface erosion (Vernant et al., 2013) and Glacial Isostatic Adjustment (Chéry et al., 2016; Mey et al., 2016). Numerical modeling shows that the isostatic response to erosion can generate the observed extensional strain pattern (Vernant et al., 2013), but the associated uplift rates are significantly smaller than the GNSS velocities (Sternai et al., 2019). On the contrary, GIA from the Last Glacial Maximum can explain the present-day uplift rates (Chéry et al., 2016; Mey et al., 2016) but a detailed comparison with horizontal deformation is lacking. In the following section, we test the compatibility of GIA models with present-day deformation of the Western Alps

3 GIA models

In order to compare GIA effects with GNSS and seismicity observations, we model the response of the lithosphere to ice loading and unloading using a simple approach of an elastic thin plate over a viscous substratum. The elastic plate flexure wm in response to the ice load is computed with the gFlex code (Wickert, 2016) using the Kirchhoff-Love thin-plate analytic solution (assuming small inline deformation, zero vertical shear, and plate rotation lower than 10°):

$$w_m(x,y) = w_{0m} kei(\frac{\sqrt{x^2+y^2}}{\alpha}) \tag{1}$$

with kei the zero-order Kelvin function, α the flexural parameter (function of the elastic plate thickness T_e and elastic parameters) and w_{0m} the maximum flexure at the center of the load (cf. Turcotte and Schubert, 2014; Wickert, 2016).

https://doi.org/10.5194/se-2021-141
Preprint. Discussion started: 14 December 2021
© Author(s) 2021. CC BY 4.0 License.

The ice load model at LGM is from Mey et al. (2016): ca. 600 km long by 200 km wide, locally up to 2 km thick (cf. Fig. 3). The postglacial rebound response is computed assuming an instantaneous ice melt after the Last Glacial Maximum (15000 yr BP) and a simple exponential decay associated with a linear viscosity of relaxation time τ_g (Turcotte and Schubert, 2014):

$$w_m(x,y,t) = w_m(x,y)e^{-t/\tau_g} \tag{2}$$

This simple 2D planar model is warranted by the relatively small spatial scale of the Alpine ice load. It comprises only two parameters: The flexural parameter α, which depends mainly on the elastic plate thickness T_e, and the characteristic time τ_g. T_e controls the spatial wavelength of the area affected by subsidence, the location of the forebulge and the maximum subsidence value (a higher T_e results in a wider a subsidence area with a lower amplitude). The characteristic time τ_g controls the relaxation speed, i.e., the time to come back to the initial pre-loading state (a higher τ_g results in a longer the postglacial rebound).

In order to test the variability of GIA predictions to these two parameters, we compute models with $5 \leq T_e \leq 100$ km and $2000 \leq \tau_g \leq 20000$ yr. Assuming that GNSS uplift rates are mostly due to GIA, comparisons between observations and model predictions indicate a best-fit parameter set ca. T_e = 10–20 km and τ_g = 4500–5500 yr (F-test statistics on residuals). Because GNSS data may be impacted by other processes (cf., above), we allow for a larger range of parameter values $5 \leq T_e \leq 40$ km and $3000 \leq \tau_g \leq 7000$ yr. These values indicate a fast and short wavelength response (low mantle velocity coupled with a thin elastic plate), in agreement with more complex models (e.g,, spatially variable plate thickness) tuned to the Western Alps (Chéry et al., 2016; Mey et al., 2016).

Stress, strain and strain rates in the elastic plate are computed from the second spatial derivative of the flexural response $w(x,y,t)$ (eq. 2) based on the Kirchhoff-Love plate theory (no vertical shear stress, only in-plane compression / tension stress). Although the actual depth and structure of the lithosphere elastic core is unknown, standard rheological models (e.g., Burov and Diament, 1995) and the shallow depth of earthquakes in the Western Alps (less than 15km; Cushing et al., 2008; Delacou et al., 2004) indicate that the seismogenic depth range is likely associated with the upper section of the model elastic plate. In order to consider the maximum GIA stress perturbations and strain rate signals, we consider hereafter the stress, strain and strain rate values computed at the top of the elastic plate. More complex situation with a decoupled two-layer elastic plate system would need to be tested with alternative models (e.g., finite element approach, Cattin et al., 2001), but we consider such complexity unlikely in the context of a thin elastic plate such as the Western Alps.

All the retained models predict similar GIA signals with compressive stress perturbations, shortening strain and extension strain rates in the Western Alps below the LGM icecap. Compressive horizontal stresses at the top of the elastic plate decrease from ca. 20–50 MPa at LGM to ca. 0–5 MPa after 15000 yr (present-day). The associated present-day extension strain rates are ca. $0.5\breve{}2.5 \times 10^{-9}$ yr^{-1}. Strain rate patterns correspond to primarily NW-SE extension rates in the inner Alps, with shortening or strike-slip rates in the Alpine foreland and surrounding regions. These patterns are shown in Fig. 3b for the model with T_e = 20 km and τ_g = 5500 yr as an example. To first order, they are consistent with the horizontal strain rates derived from GNSS data (cf. Fig. 3b vs. 3c). Additional model predictions are shown in the Supplementary Material A3 for illustration.

https://doi.org/10.5194/se-2021-141
Preprint. Discussion started: 14 December 2021
© Author(s) 2021. CC BY 4.0 License.

More specifically, the extension rate area is centered on the LGM icecap extent, approximately 150 km wide in the Central Alps and 300 km wide in the Western Alps. At the Switzerland-Italy border and in the French Alps, modeled and GNSS strain rates are consistent both in direction (rotation from N-S to NNW-SSE) and in amplitudes. In the Switzerland-Italy border area, the modeled values range are about $0.9\breve{}2.1 \times 10^{-9}$ yr^{-1} while the GNSS data indicates $(2.5 \pm 1) \times 10^{-9}$ yr^{-1}. In the French Alps, the model rates range between 0.4 and 0.8×10^{-9} yr^{-1} in agreement with the $(0.9 \pm 0.7) \times 10^{-9}$ yr^{-1} given by the GNSS measurements. Based on these results, GIA accounts for a minimum of 30% and up to 100% of the GNSS extension rates.

In contrast, the GIA models are unable to reproduce the GNSS $(0.8 \pm 1) \times 10^{-9}$ yr^{-1} E-W extension rates in Italy or the $(1.5 \pm 1) \times 10^{-9}$ yr^{-1} strike slip strain rates along the southern France-Italy border. This area being located south of the Adria / Eurasia rotation pole, we propose that these strain rates may be in part related to Adria micro-plate kinematics, consistent with the $0.3 - 0.8$ mm.yr^{-1} of E-W extension in southern Western Alps (e.g., Nocquet, 2012).

The inner Western Alps extension is surrounded by radial shortening in the Rhine Graben, Jura Mountains and Rhone Valley regions. In the Rhine graben and Jura, the GIA modeled shortening rate directions are consistent with the GNSS strain rates, but the amplitudes are about three times smaller. This suggests that the shortening rates in these regions cannot be solely attributed to Alpine GIA; processes such as Scandinavian postglacial rebound (Nocquet et al., 2005) or a buoyant mantle plume located beneath Eifel volcanic area (Kreemer et al., 2020) may contribute to the shortening signal.

4 GIA stress perturbations on active faults

As expected from the conceptual flexural model (Fig. 1), the GIA stress perturbations correspond to horizontal compressive stress: uniaxial NW-SE compression in southern Switzerland, near-isotropic compression on the French Alps, and E-W uniaxial compression in the Southern Alps (French-Italian border). As previously mentioned, strain rate and stress present opposite signs and these maximum GIA compression (Fig. 4a) are located at the maximum GIA extension rate (Fig. 3c).

The impact of GIA stress perturbations on faults is estimated using the Coulomb failure criterion based on the fault azimuth and dip angle. The Coulomb Failure Stress Δ_{CFS} is computed based on the fault shear and normal stress (e.g., King et al., 1994):

$$\Delta_{CFS} = \tau - \mu^{'} \sigma_n \tag{3}$$

with $\mu^{'}$ the effective coefficient of friction (between 0.1 and 0.6), τ the shear stress and σ_n the normal stress. The fault-slip style associated with this stress perturbation is given by the rake r:

$$r = arctan(\frac{\tau_d}{\tau_s}) \tag{4}$$

with τ_d and τ_s the fault shear stress along dip and azimuth directions, respectively. In all models, these Coulomb Failure Stress and rake represent the effect of the GIA stress perturbations and can be interpreted as GIA favoring a specific fault style

https://doi.org/10.5194/se-2021-141
Preprint. Discussion started: 14 December 2021
© Author(s) 2021. CC BY 4.0 License.

at a given stress level if $\Delta_{CFS} < 0$, or GIA inhibiting fault motion if $\Delta_{CFS} > 0$.

Figure 4b presents the computed rakes for three sets of typical faults in the Western Alps (Fig. 4a): the Vuache Fault, the Belledonne Fault, and a series of potential faults representative of normal-faulting earthquakes in the Internal Massifs above the Penninic Front (hereafter IMNF, Inner Massifs Normal Faults; Sue et al., 2003, 1999). The fault geometries are extracted from the BDFA and neotectonic databases (Grellet, 1993; Jomard et al., 2017). Due to the uncertainties on the dip angles, several values are tested (30–80°). In Figure 4b, the GIA model rakes are shown as boxplots that represent the variability in GIA model parameters (T_e and τ_g) and fault geometries (azimuth and dip). The predicted rakes compared to those derived from earthquake focal mechanisms.

The GIA Coulomb Failure Stress perturbation depends on the fault geometry and the assumed effective friction (eq. 3). Models with standard friction ($\mu^{'}$ = 0.6) and near-vertical fault dips results in negative Δ_{CFS} in dictating that GIA tends to inhibit fault rupture in these cases. In contrast, models with low effective friction ($\mu^{'}$ = 0.1) or low fault dips result in mostly positive Δ_{CFS} between 0.1 and 2 MPa. These models are associated with fault-slip rakes corresponding to reverse faulting (rakes r = 50–110, Fig. 4b). This faulting style is opposite to that observed in the focal mechanisms along the IMNF (Delacou et al., 2004; Mathey et al., 2021; Sue et al., 1999). For the Belledonne Fault, the GIA stress perturbation favors reverse faulting (r = 60–130) while the focal mechanisms show right-lateral strike-slip (r = 180 $\pm$ 20; Thouvenot et al., 2003). The Vuache Fault orientation is strongly oblique to the GIA stress field (Fig. 4a), with the northern part of the fault located in a transition zone where the GIA stress is almost zero. Predicted rakes vary between 60 and 150 (reverse faulting), inconsistent with the observed left-lateral faulting style (Rabin et al., 2018). In these three cases, GIA Δ_{CFS} perturbations can reach up to 1–2 MPa, a level commonly considered sufficient to trigger preloaded fault rupture (e.g., King et al., 1994; Steer et al., 2014; Stein, 1999), but the modeled rakes are systematically different from the observed ones. Thus, GIA in the Western Alps cannot explain the kinematics of the aforementioned faults.

The effect of GIA is more difficult to identify for structures parallel to the main stress direction. Along the Durance Fault, in the southern Western Alps, the GIA extensive NE-SW stress perturbations decrease from 0.35-0.7 MPa in the area north of the fault to 0.15-0.25 MPa around the southern segment (Fig. 5a). Due to the bends in the Durance Fault trace, the range of predicted rakes is very large for this fault (Fig. 5b). Δ_{CFS} are systematically positive (with low effective friction $\mu^{'}$ = 0.1). For the northern half, GIA modeled rakes vary from 0°to 180°indicating that, depending on the fault segment orientation, the kinematics can be reverse, left-lateral, or right-lateral. For the southern half, GIA stress perturbations predict a right-lateral strike-slip motion. The focal mechanisms along the Durance Fault system suggest mostly left-lateral displacements (Cushing et al., 2008). Thus, rupture on some segments may be promoted by the GIA stress perturbations, whereas others are clearly inhibited (Fig. 5b).

https://doi.org/10.5194/se-2021-141
Preprint. Discussion started: 14 December 2021
© Author(s) 2021. CC BY 4.0 License.

5 GIA explains present-day Western Alps GNSS deformation but not seismicity

As shown by several studies in the last decade, GNSS deformation rates in the Western Alps correspond to vertical uplift rates ca. 1–2 mm.yr^{-1} and horizontal extension rates ca. $(1\breve{}3) \times 10^{-9}$ yr^{-1} (e.g., Masson et al., 2019; Walpersdorf et al., 2018). These deformation rates are compatible with GIA signal from the Last Glacial Maximum provided the Western Alps behave mechanically as a thin elastic plate (T_e = 10–35 km) over a low viscosity mantle (τ_g = 4500–8000 yr) (e.g., Chéry et al., 2016; Mey et al., 2016, cf. Fig.3). Although the actual contribution of GIA relative to other processes (e.g., slab breakoff, erosion) is debated (Sternai et al., 2019), the good agreement between simple GIA model predictions and the observed GNSS uplift rates and horizontal strain rates suggests that GIA is a major contributor to those observed deformation rates, at least in the region below the LGM icecap. The compatibility between the GNSS strain rates and the seismicity deformation style has led several authors to consider GNSS data as a constraint on seismicity budget (e.g., Sue et al., 2007; Walpersdorf et al., 2018, 2015).

Yet, our analysis shows that GIA stress perturbations in the Western Alps either inhibit fault rupture ($\Delta_{CFS} < 0$) or are inconsistent with the deformation pattern highlighted by earthquake focal mechanisms (cf., Figs. 4 and 5). The overall GIA stress perturbations correspond to horizontal compression that would favor reverse to strike-slip faulting styles, opposite to the normal faulting style observed in the region. In fact, Coulomb Failure Stress analyses show that GIA stress perturbations tend to inhibit the observed faulting style for large faults in the Western Alps (such as the Belledonne Fault).

Our study shows an apparent strain rate - stress paradox, wherein GIA can explain the observed most of GNSS strain rates but not the seismicity. This apparent paradox is easily resolved by considering that the observed (and modeled) horizontal extension rates are merely a diminution over time of the compression / shortening induced at surface of the lithosphere by its downward flexure under the LGM ice load. This situation is similar to that observed in the forearcs of subduction zones where a stress orientations and styles may differ from the strain rate patterns, the latter being transient signals due to the interseismic locking of the subduction fault (Wang, 2000).

A similar situation has been studied by Craig et al. (2016) for Fennoscandia and its early-postglacial reverse-faulting earthquakes. They argue that these reverse earthquakes occurred during a period of GIA extension strain rates, and thus were the expression of compressive stress stored in the lithosphere over a long (tectonic) time. This analysis relies on the assumption that faults are sensitive to the stress rate of change since the LGM (reduction of compressive stress = extensional stress rate), when in fact the full GIA stress perturbation remains compressive throughout the whole glacial cycle (up to present-day), thus promoting reverse faulting earthquakes as proposed by previous studies (Hampel et al., 2009; Steffen et al., 2014; Wu et al., 1999).

Coming back to the Western Alps case, the opposite style between the GIA strain rates and stress perturbations results in a particular situation. GIA is likely the cause of a large part (over 50%) of the observed geodetic strain rates, but it tends to inhibit the current seismicity and its arc-perpendicular extension. Thus, although it may be tempting to do so, GNSS strain rates cannot be used in seismicity rates or seismic hazard analyses in this context. Our results point out the necessity for an additional mechanism (or several additional mechanisms) that can be the cause of the arc-perpendicular extension pattern expressed in the earthquake focal mechanisms (e.g., Holocene or Quaternary erosion, slab tear, etc.). In this situation, the long-term horizontal

https://doi.org/10.5194/se-2021-141
Preprint. Discussion started: 14 December 2021
© Author(s) 2021. CC BY 4.0 License.

extension stress pattern can be modulated by the GIA stress perturbations, with a reduction of the deformation and earthquake activity during the glacial period and an increase in activity after the glacial maximum (cf. Hampel et al., 2009; Steffen et al., 2014). The integration of GIA stress perturbations in seismicity and seismic hazard studies would thus require mechanical models and cannot be simply based on direct GNSS strain rate integration.

Code and data availability. Maps have been made with GMT6. Figure 4b and 5b were performed with python 3.6 (Python Software Foundation), as well as models presented in the article. GPS velocities field has been processed by C. Masson using CCRS-PPP (details in Masson (2019)).Flexure is computed from gFlex code (Wickert, 2016) and glex_load code (https://github.com/juliettegroset/gflex_load.git). GPS velocities field has been processed by C. Masson using CCRS-PPP (details in Masson (2019)).

Appendix A

A1 Horizontal Velocity field

The velocity field (Fig. A1) is from Masson (2019). The analysis has been made on 1443 permanent stations spread on western Europe in Precise Point Positioning (PPP) from CSRS-PPP software (Kouba and Héroux, 2001). The detail of the method is described in Masson (2019).

A2 Gaussian filtering method

The smoothed velocity field is computed on a regular grid (0.5×0.5 degree). The velocity on each grid point is computed from velocity vectors of all GNSS stations, weighted according to their distance with a Gaussian function (Mazzotti et al., 2011). The velocity vector at each point of the grid V_g is defined by:

$$V_{gi} = \frac{(\sum_{n=1}^{N} \frac{G_n}{\sigma_{ni}^2} V_{ni})}{(\sum_{n=1}^{N} \frac{G_n}{\sigma_{ni}^2})} \tag{A1}$$

With i the component (North, East, Up), N the number of stations, V_n the velocity vector at the station n and σ the uncertainty of the velocity component. G_n is defined by the Gaussian function parameters r_g (the Gaussian half-width), and Δ_n the distance between stations and grid point:

$$G_n = e^{-log(2)\frac{\Delta_n^2}{r_g^2}} \tag{A2}$$

The velocity Gaussian function grid is differentiated to obtain the strain rate tensor at each point. The effect of Gaussian half-width r_g on the noise in the final solution is shown in fig. A2.

https://doi.org/10.5194/se-2021-141
Preprint. Discussion started: 14 December 2021
© Author(s) 2021. CC BY 4.0 License.

A3 Additional models

The variability of tested models (depending on the elastic thickness T_e and the characteristic time τ_{ve}) is investigated in fig. A3 and A4. T_e control the spatial size of the flexure, τ_g control the present-day amplitude of the response. On fig. A4, models (a) and (d) show respectively the maximum and the minimum stress perturbation.

Author contributions. JG and SM developed the gflex_load code. JG has computed the models. JG, SM, and PV interpreted the results and wrote the article.

Competing interests. The authors declare that they have no conflict of interest.

Acknowledgements. This work was supported by EDF through the DEFORM_3D project (SIGMA2 program). We thank T. Camelbeeck and Y. Klinger for their suggestions during the SIGMA2 scientific committee. We also thank R. Steffen for the discussion about this work and J. Mey for sharing with us his ice-cap model. Thanks to M. Gamelin for her implication in her Master's internship that initiated this work.

https://doi.org/10.5194/se-2021-141
Preprint. Discussion started: 14 December 2021
© Author(s) 2021. CC BY 4.0 License.

References

Battaglia, M., Murray, M. H., Serpelloni, E., and Bürgmann, R.: The Adriatic Region: An Independent Microplate within the Africa-Eurasia Collision Zone: THE ADRIATIC REGION, Geophysical Research Letters, 31, n/a–n/a, https://doi.org/10.1029/2004GL019723, 2004.

Billant, J., Hippolyte, J.-C., and Bellier, O.: Tectonic and Geomorphic Analysis of the Belledonne Border Fault and Its Extensions, Western Alps, Tectonophysics, 659, 31–52, https://doi.org/10.1016/j.tecto.2015.07.025, 2015.

Burov, E. B. and Diament, M.: The Effective Elastic Thickness (T e) of Continental Lithosphere: What Does It Really Mean?, Journal of Geophysical Research: Solid Earth, 100, 3905–3927, https://doi.org/10.1029/94JB02770, 1995.

Calais, E., Camelbeeck, T., Stein, S., Liu, M., and Craig, T. J.: A New Paradigm for Large Earthquakes in Stable Continental Plate Interiors, Geophysical Research Letters, 43, 10,621–10,637, https://doi.org/10.1002/2016GL070815, 2016.

Cara, M., Cansi, Y., Schlupp, A., Arroucau, P., Béthoux, N., Beucler, E., Bruno, S., Calvet, M., Chevrot, S., Deboissy, A., Delouis, B., Denieul, M., Deschamps, A., Doubre, C., Fréchet, J., Godey, S., Golle, O., Grunberg, M., Guilbert, J., Haugmard, M., Jenatton, L., Lambotte, S., Leobal, D., Maron, C., Mendel, V., Merrer, S., Macquet, M., Mignan, A., Mocquet, A., Nicolas, M., Perrot, J., Potin, B., Sanchez, O., Santoire, J.-P., Sèbe, O., Sylvander, M., Thouvenot, F., Woerd, J. V. D., and Woerd, K. V. D.: SI-Hex: A New Catalogue of Instrumental Seismicity for Metropolitan France, Bulletin de la Société Géologique de France, 186, 3–19, https://doi.org/10.2113/gssgfbull.186.1.3, 2015.

Cattin, R., de Chabalier, J., King, G., Vigny, C., Avouac, J., and Ruegg, J.: Thermo-Mechanical Modeling of Seismic Cycle and Quaternary Deformation of the Asal Rift, Djibouti, Africa: Implication for the Rheology of the Lithosphere, 2001, T51B–0870, 2001.

Chéry, J., Genti, M., and Vernant, P.: Ice Cap Melting and Low-viscosity Crustal Root Explain the Narrow Geodetic Uplift of the Western Alps, Geophysical Research Letters, 43, 3193–3200, https://doi.org/10.1002/2016GL067821, 2016.

Craig, T. J., Calais, E., Fleitout, L., Bollinger, L., and Scotti, O.: Evidence for the Release of Long-Term Tectonic Strain Stored in Continental Interiors through Intraplate Earthquakes, Geophysical Research Letters, 43, 6826–6836, https://doi.org/10.1002/2016GL069359, 2016.

Cushing, E. M., Bellier, O., Nechtschein, S., Sébrier, M., Lomax, A., Volant, P., Dervin, P., Guignard, P., and Bove, L.: A Multidisciplinary Study of a Slow-Slipping Fault for Seismic Hazard Assessment: The Example of the Middle Durance Fault (SE France), Geophysical Journal International, 172, 1163–1178, https://doi.org/10.1111/j.1365-246X.2007.03683.x, 2008.

D'Agostino, N., Avallone, A., Cheloni, D., D'Anastasio, E., Mantenuto, S., and Selvaggi, G.: Active Tectonics of the Adriatic Region from GPS and Earthquake Slip Vectors, Journal of Geophysical Research: Solid Earth, 113, https://doi.org/10.1029/2008JB005860, 2008.

Delacou, B., Sue, C., Champagnac, J.-D., and Burkhard, M.: Present-Day Geodynamics in the Bend of the Western and Central Alps as Constrained by Earthquake Analysis, Geophysical Journal International, 158, 753–774, https://doi.org/10.1111/j.1365-246X.2004.02320.x, 2004.

Grellet, B.: Sismotectonique de La France Métropolitaine Dans Son Cadre Géologique et Géophysique: Avec Atlas de 23 Cartes Au 1/4 000 000ème et Une Carte Au 1/1 000 000ème, 1993.

Hampel, A., Hetzel, R., Maniatis, G., and Karow, T.: Three-Dimensional Numerical Modeling of Slip Rate Variations on Normal and Thrust Fault Arrays during Ice Cap Growth and Melting, Journal of Geophysical Research, 114, B08 406, https://doi.org/10.1029/2008JB006113, 2009.

Hetzel, R. and Hampel, A.: Slip Rate Variations on Normal Faults during Glacial–Interglacial Changes in Surface Loads, Nature, 435, 81–84, https://doi.org/10.1038/nature03562, 2005.

Johansson, J. M., Davis, J. L., Scherneck, H.-G., Milne, G. A., Vermeer, M., Mitrovica, J. X., Bennett, R. A., Jonsson, B., Elgered, G., Elósegui, P., Koivula, H., Poutanen, M., Rönnäng, B. O., and Shapiro, I. I.: Continuous GPS Measurements of Postglacial Adjustment in Fennoscandia 1. Geodetic Results, Journal of Geophysical Research: Solid Earth, 107, ETG 3–1–ETG 3–27, https://doi.org/10.1029/2001JB000400, 2002.

Johnston, A. C.: Suppression of Earthquakes by Large Continental Ice Sheets, Nature, https://doi.org/10.1038/330467a0, 1987.

Jomard, H., Cushing, E. M., Palumbo, L., Baize, S., David, C., and Chartier, T.: Transposing an Active Fault Database into a Seismic Hazard Fault Model for Nuclear Facilities – Part 1: Building a Database of Potentially Active Faults (BDFA) for Metropolitan France, Natural Hazards and Earth System Sciences, 17, 1573–1584, https://doi.org/10.5194/nhess-17-1573-2017, 2017.

King, G. C. P., Stein, R. S., and Lin, J.: Static Stress Changes and the Triggering of Earthquakes, Bulletin of the Seismological Society of America, 84, 935–953, 1994.

Kouba, J. and Héroux, P.: Precise Point Positioning Using IGS Orbit and Clock Products, GPS Solutions, 5, 12–28, https://doi.org/10.1007/PL00012883, 2001.

Kreemer, C., Blewitt, G., and Davis, P. M.: Geodetic Evidence for a Buoyant Mantle Plume beneath the Eifel Volcanic Area, NW Europe, Geophysical Journal International, 222, 1316–1332, https://doi.org/10.1093/gji/ggaa227, 2020.

Larroque, C., Scotti, O., and Ioualalen, M.: Reappraisal of the 1887 Ligurian Earthquake (Western Mediterranean) from Macroseismicity, Active Tectonics and Tsunami Modelling, Geophysical Journal International, 190, 87–104, https://doi.org/10.1111/j.1365-246X.2012.05498.x, 2012.

Masson, C.: Improvement of GPS Analysis Methods for Intraplate Deformation Studies : Example of France, Theses, Université Montpellier, 2019.

Masson, C., Mazzotti, S., Vernant, P., and Doerflinger, E.: Extracting Small Deformation beyond Individual Station Precision from Dense Global Navigation Satellite System (GNSS) Networks in France and Western Europe, Solid Earth, 10, 1905–1920, https://doi.org/10.5194/se-10-1905-2019, 2019.

Mathey, M., Sue, C., Pagani, C., Baize, S., Walpersdorf, A., Bodin, T., Husson, L., Hannouz, E., and Potin, B.: Present-Day Geodynamics of the Western Alps: New Insights from Earthquake Mechanisms, Solid Earth, 12, 1661–1681, https://doi.org/10.5194/se-12-1661-2021, 2021.

Mazzotti, S., James, T. S., Henton, J., and Adams, J.: GPS Crustal Strain, Postglacial Rebound, and Seismic Hazard in Eastern North America: The Saint Lawrence Valley Example, Journal of Geophysical Research: Solid Earth, 110, https://doi.org/10.1029/2004JB003590, 2005.

Mazzotti, S., Leonard, L. J., Cassidy, J. F., Rogers, G. C., and Halchuk, S.: Seismic Hazard in Western Canada from GPS Strain Rates versus Earthquake Catalog, Journal of Geophysical Research: Solid Earth, 116, https://doi.org/10.1029/2011JB008213, 2011.

Meghraoui, M., Delouis, B., Ferry, M., Giardini, D., Huggenberger, P., Spottke, I., and Granet, M.: Active Normal Faulting in the Upper Rhine Graben and Paleoseismic Identification of the 1356 Basel Earthquake, Science, 293, 2070–2073, https://doi.org/10.1126/science.1010618, 2001.

Mey, J., Scherler, D., Wickert, A. D., Egholm, D. L., Tesauro, M., Schildgen, T. F., and Strecker, M. R.: Glacial Isostatic Uplift of the European Alps, Nature Communications, 7, 1–10, https://doi.org/10.1038/ncomms13382, 2016.

Nguyen, H., Vernant, P., Mazzotti, S., Khazaradze, G., and Asensio Ferreira, E.: 3D GPS Velocity Field and Its Implications on the Present-Day Postorogenic Deformation of the Western Alps and Pyrenees, 2016.

Nocquet, J.-M.: Present-Day Kinematics of the Mediterranean: A Comprehensive Overview of GPS Results, Tectonophysics, 579, 220–242, https://doi.org/10.1016/j.tecto.2012.03.037, 2012.

Nocquet, J.-M., Calais, E., and Parsons, B.: Geodetic Constraints on Glacial Isostatic Adjustment in Europe, Geophysical Research Letters, 32, https://doi.org/10.1029/2004GL022174, 2005.

Nocquet, J.-M., Sue, C., Walpersdorf, A., Tran, T., Lenôtre, N., Vernant, P., Cushing, M., Jouanne, F., Masson, F., Baize, S., Chéry, J., and van der Beek, P. A.: Present-Day Uplift of the Western Alps, Scientific Reports, 6, 28 404, https://doi.org/10.1038/srep28404, 2016.

Peltier, W. R., Argus, D. F., and Drummond, R.: Space Geodesy Constrains Ice Age Terminal Deglaciation: The Global ICE-6G_C (VM5a) Model, Journal of Geophysical Research: Solid Earth, 120, 450–487, https://doi.org/10.1002/2014JB011176, 2015.

Rabin, M., Sue, C., Walpersdorf, A., Sakic, P., Albaric, J., and Fores, B.: Present-Day Deformations of the Jura Arc Inferred by GPS Surveying and Earthquake Focal Mechanisms, Tectonics, 37, 3782–3804, https://doi.org/10.1029/2018TC005047, 2018.

Steer, P., Simoes, M., Cattin, R., and Shyu, J. B. H.: Erosion Influences the Seismicity of Active Thrust Faults, Nature Communications, 5, 5564, https://doi.org/10.1038/ncomms6564, 2014.

Steffen, R., Wu, P., Steffen, H., and Eaton, D. W.: The Effect of Earth Rheology and Ice-Sheet Size on Fault Slip and Magnitude of Postglacial Earthquakes, Earth and Planetary Science Letters, 388, 71–80, https://doi.org/10.1016/j.epsl.2013.11.058, 2014.

Stein, R. S.: The Role of Stress Transfer in Earthquake Occurrence, Nature, 402, 605–609, https://doi.org/10.1038/45144, 1999.

Sternai, P., Sue, C., Husson, L., Serpelloni, E., Becker, T. W., Willett, S. D., Faccenna, C., Di Giulio, A., Spada, G., Jolivet, L., Valla, P., Petit, C., Nocquet, J.-M., Walpersdorf, A., and Castelltort, S.: Present-Day Uplift of the European Alps: Evaluating Mechanisms and Models of Their Relative Contributions, Earth-Science Reviews, 190, 589–604, https://doi.org/10.1016/j.earscirev.2019.01.005, 2019.

Stucchi, M., Rovida, A., Gomez Capera, A. A., Alexandre, P., Camelbeeck, T., Demircioglu, M. B., Gasperini, P., Kouskouna, V., Musson, R. M. W., Radulian, M., Sesetyan, K., Vilanova, S., Baumont, D., Bungum, H., Fäh, D., Lenhardt, W., Makropoulos, K., Martinez Solares, J. M., Scotti, O., Živčić, M., Albini, P., Batllo, J., Papaioannou, C., Tatevossian, R., Locati, M., Meletti, C., Viganò, D., and Giardini, D.: The SHARE European Earthquake Catalogue (SHEEC) 1000–1899, Journal of Seismology, 17, 523–544, https://doi.org/10.1007/s10950-012-9335-2, 2013.

Sue, C., Thouvenot, F., Fréchet, J., and Tricart, P.: Widespread Extension in the Core of the Western Alps Revealed by Earthquake Analysis, Journal of Geophysical Research: Solid Earth, 104, 25 611–25 622, https://doi.org/10.1029/1999JB900249, 1999.

Sue, C., Delacou, B., Champagnac, J. D., and Burkhard, M.: Quantification of the Seismic Strain in the Western Alps, p. 10241, 2003.

Sue, C., Delacou, B., Champagnac, J.-D., Allanic, C., and Burkhard, M.: Aseismic Deformation in the Alps: GPS vs. Seismic Strain Quantification, Terra Nova, 19, 182–188, https://doi.org/10.1111/j.1365-3121.2007.00732.x, 2007.

Talwani, P.: On the Nature of Intraplate Earthquakes, Journal of Seismology, 21, 47–68, https://doi.org/10.1007/s10950-016-9582-8, 2017.

Tarayoun, A.: Localisation de La Déformation et de La Sismicité En Domaine Intraplaque : Réactivation Des Paléo-Structures Crustales et Lithosphériques, Thesis, Montpellier, 2018.

Thouvenot, F., Fréchet, J., Tapponnier, P., Thomas, J.-C., Le Brun, B., Ménard, G., Lacassin, R., Jenatton, L., Grasso, J.-R., Coutant, O., Paul, A., and Hatzfeld, D.: The ML 5.3 Epagny (French Alps) Earthquake of 1996 July 15: A Long-Awaited Event on the Vuache Fault, Geophysical Journal International, 135, 876–892, https://doi.org/10.1046/j.1365-246X.1998.00662.x, 1998.

Thouvenot, F., Fréchet, J., Jenatton, L., and Gamond, J.-F.: The Belledonne Border Fault: Identification of an Active Seismic Strike-Slip Fault in the Western Alps, Geophysical Journal International, 155, 174–192, https://doi.org/10.1046/j.1365-246X.2003.02033.x, 2003.

Turcotte, D. L. and Schubert, G.: Geodynamics, Cambridge University Press, Cambridge, United Kingdom, third edition edn., 2014.

Vernant, P., Hivert, F., Chéry, J., Steer, P., Cattin, R., and Rigo, A.: Erosion-Induced Isostatic Rebound Triggers Extension in Low Convergent Mountain Ranges, Geology, 41, 467–470, https://doi.org/10.1130/G33942.1, 2013.

https://doi.org/10.5194/se-2021-141
Preprint. Discussion started: 14 December 2021
© Author(s) 2021. CC BY 4.0 License.

Walpersdorf, A., Sue, C., Baize, S., Cotte, N., Bascou, P., Beauval, C., Collard, P., Daniel, G., Dyer, H., Grasso, J. R., Hautecoeur, O., Helmstetter, A., Hok, S., Langlais, M., Menard, G., Mousavi, Z., Ponton, F., Rizza, M., Rolland, L., Souami, D., Thirard, L., Vaudey, P., Voisin, C., and Martinod, J.: Coherence between Geodetic and Seismic Deformation in a Context of Slow Tectonic Activity (SW Alps, France), Journal of Geodynamics, 85, 58–65, https://doi.org/10.1016/j.jog.2015.02.001, 2015.

Walpersdorf, A., Pinget, L., Vernant, P., Sue, C., and Deprez, A.: Does Long-Term GPS in the Western Alps Finally Confirm Earthquake Mechanisms?, Tectonics, 37, 3721–3737, https://doi.org/10.1029/2018TC005054, 2018.

Wang, K.: Stress–Strain 'Paradox', Plate Coupling, and Forearc Seismicity at the Cascadia and Nankai Subduction Zones, Tectonophysics, 319, 321–338, https://doi.org/10.1016/S0040-1951(99)00301-7, 2000.

Wickert, A. D.: Open-Source Modular Solutions for Flexural Isostasy: gFlex v1.0, Geoscientific Model Development, 9, 997–1017, https://doi.org/10.5194/gmd-9-997-2016, 2016.

Wu, P. and Hasegawa, H. S.: Induced Stresses and Fault Potential in Eastern Canada Due to a Realistic Load: A Preliminary Analysis, Geophysical Journal International, 127, 215–229, https://doi.org/10.1111/j.1365-246X.1996.tb01546.x, 1996.

Wu, P., Johnston, P., and Lambeck, K.: Postglacial Rebound and Fault Instability in Fennoscandia, Geophysical Journal International, 139, 657–670, https://doi.org/10.1046/j.1365-246x.1999.00963.x, 1999.

https://doi.org/10.5194/se-2021-141
Preprint. Discussion started: 14 December 2021
© Author(s) 2021. CC BY 4.0 License.

Solid Earth Discussions
Open Access
EGU

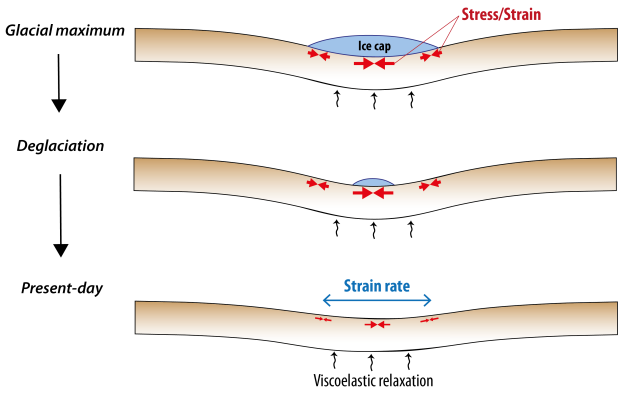

Figure 1. Conceptual model of Glacial Isostatic Adjustment (GIA) induced stress, strain and strain.

https://doi.org/10.5194/se-2021-141
Preprint. Discussion started: 14 December 2021
© Author(s) 2021. CC BY 4.0 License.

Solid Earth Discussions
Open Access
EGU

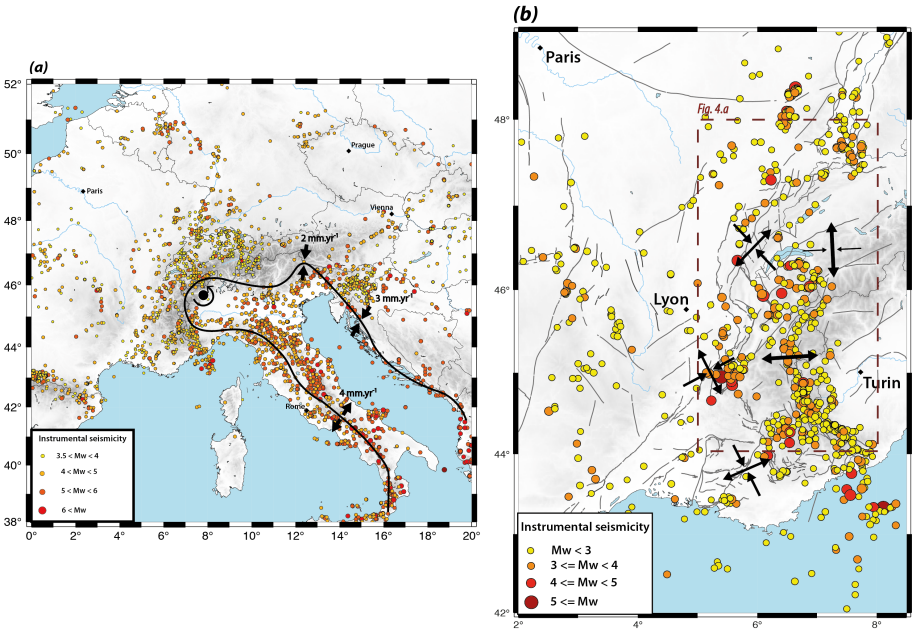

Figure 2. (a) Instrumental seismicity of western Europe (catalogs: SI-HEX, Cara et al. (2015); SHARE, Stucchi et al. (2013)). Predicted Adria micro-plate motion relative to Eurasia represented along the Adria border. (b) Instrumental seismicity in Western Alps (Cara et al., 2015) and interpreted seismic strain style from focal mechanisms (associated with Vuache fault (Rabin et al., 2018), Belledonne fault (Thouvenot et al., 2003) and old structures such as Penninic Front Thrust faults (Sue et al., 2003, 1999).

https://doi.org/10.5194/se-2021-141
Preprint. Discussion started: 14 December 2021
© Author(s) 2021. CC BY 4.0 License.

Solid Earth Discussions
Open Access
EGU

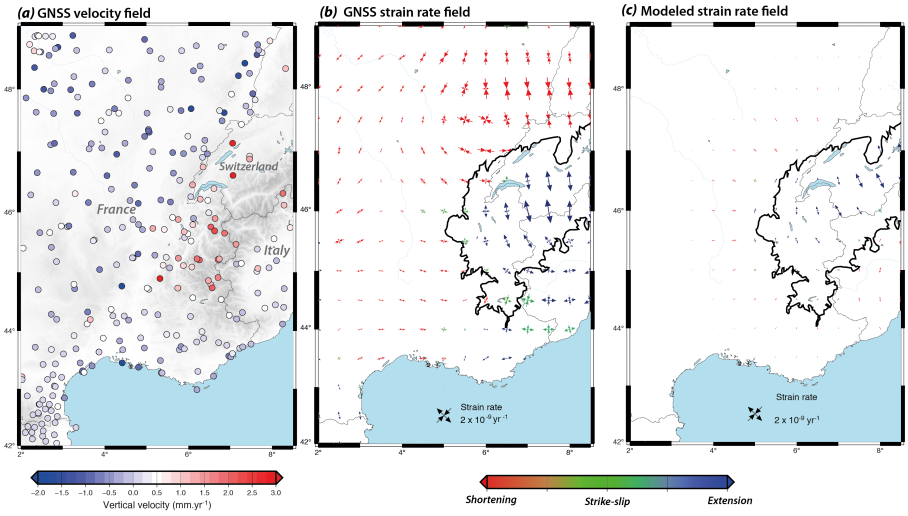

Figure 3. (a) Vertical velocity field from GNSS permanent networks (Masson, 2019) and (b) strain rate field extracted from Gaussian Smoothing method (half-width of 90 km); (c) Best-fit GIA model strain rate field (T_e = 20 km ; τ_g = 5500 yr). Black line is Last Glacial Maximum ice extension (Mey et al., 2016).

https://doi.org/10.5194/se-2021-141
Preprint. Discussion started: 14 December 2021
© Author(s) 2021. CC BY 4.0 License.

Solid Earth Discussions
Open Access
EGU

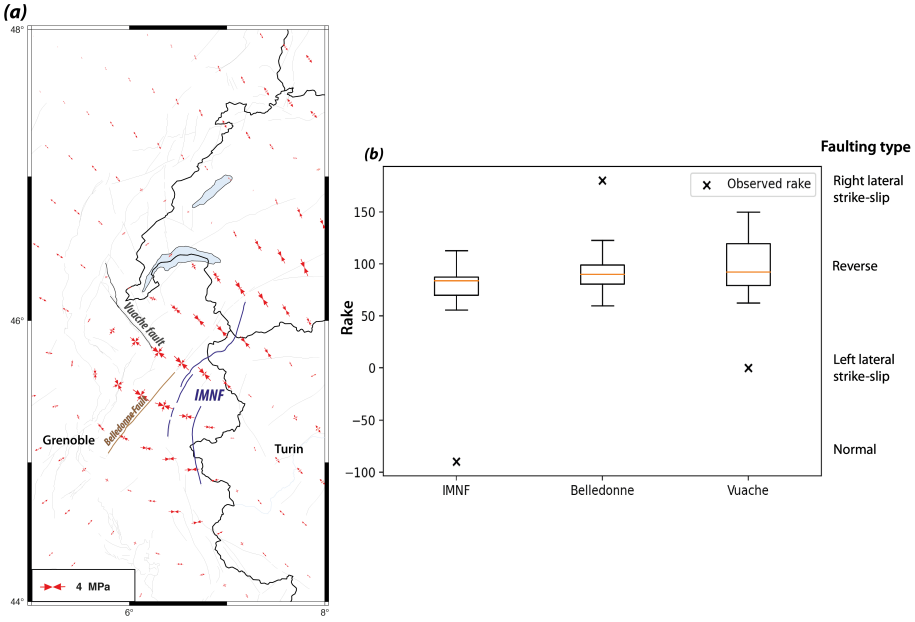

Figure 4. (a) Horizontal GIA stress perturbations (model with T_e=20km ; τ_g = 5500 yr) and fault sets used in the comparison. (b) GIA model rakes (boxplot) and observed rakes (black cross, from Billant et al. (2015); Delacou et al. (2004); Rabin et al. (2018); Sue et al. (1999); Thouvenot et al. (2003))

https://doi.org/10.5194/se-2021-141
Preprint. Discussion started: 14 December 2021
© Author(s) 2021. CC BY 4.0 License.

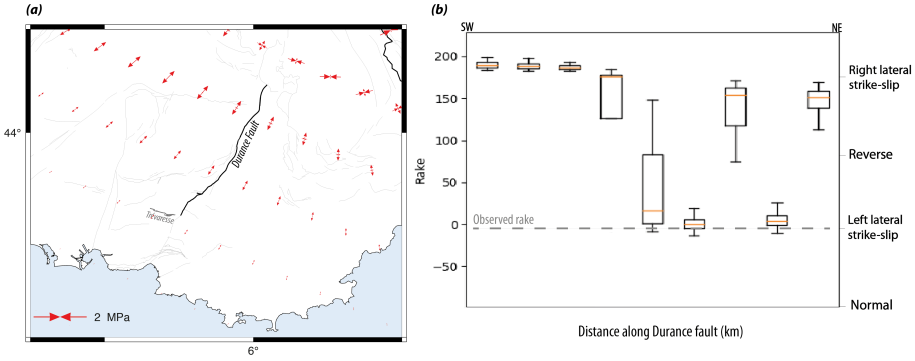

Figure 5. GIA stress perturbation. (a) Horizontal stress perturbations (model with T_e=20km ; τ_g = 5500 yr) and fault used in the comparison. (b) GIA model rakes (boxplot) and observed rake along Durance fault, from south-western to north-eastern border. Observed rake are deduces with focal mechanism (Cushing et al., 2008).

https://doi.org/10.5194/se-2021-141
Preprint. Discussion started: 14 December 2021
© Author(s) 2021. CC BY 4.0 License.

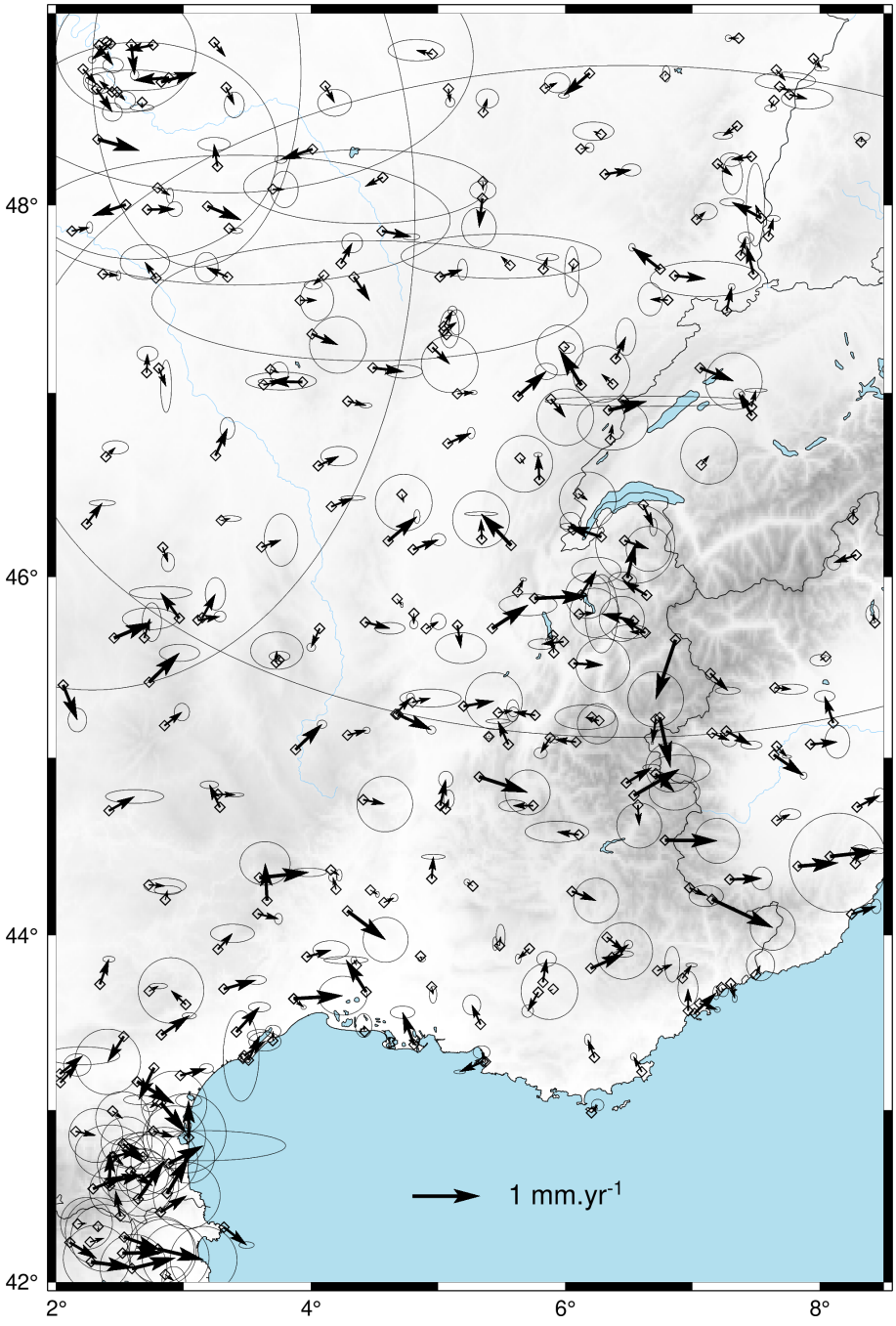

Figure A1. Horizontal velocity field from permanent GNSS network (Masson, 2019). Ellipses represent unvertainties.

https://doi.org/10.5194/se-2021-141
Preprint. Discussion started: 14 December 2021
© Author(s) 2021. CC BY 4.0 License.

Solid Earth Discussions
Open Access
EGU

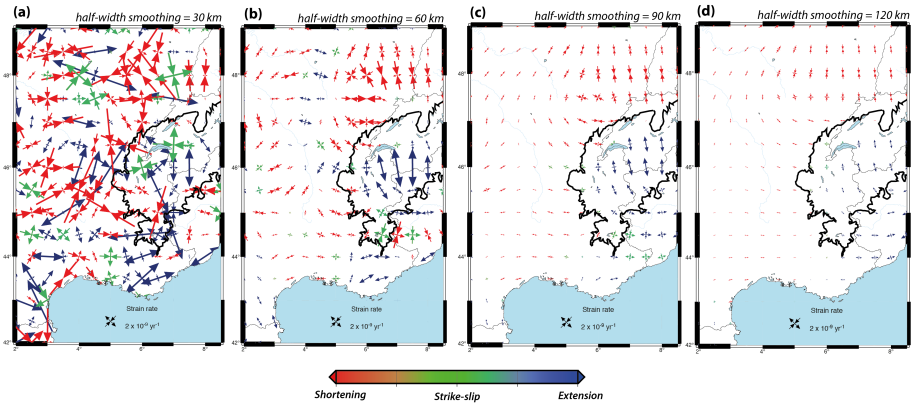

Figure A2. Strain rate fields extracted from Masson (2019) velocity field, with Gaussian filtering method with a half-width distance of (a) r_g = 30 km, (b) r_g = 60 km, (c) r_g = 9 0km and (d) r_g =120 km. Black line is Last Glacial Maximum ice extension (Mey et al., 2016).

https://doi.org/10.5194/se-2021-141
Preprint. Discussion started: 14 December 2021
© Author(s) 2021. CC BY 4.0 License.

Solid Earth Discussions
Open Access
EGU

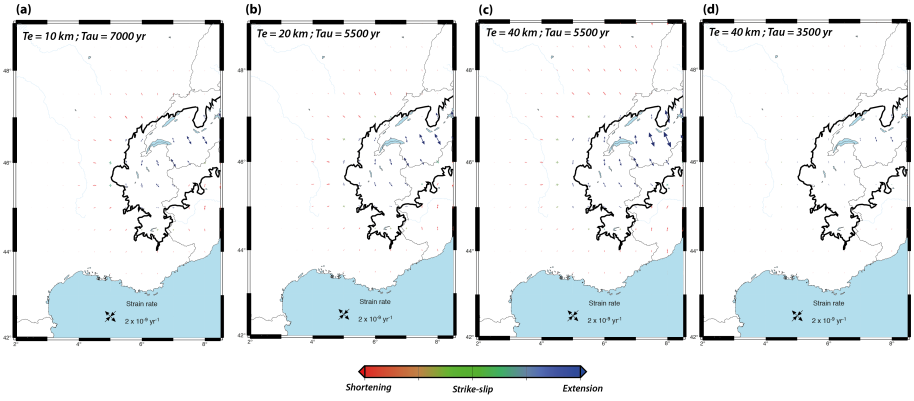

Figure A3. GIA modeled strain rate fields (a) T_e = 10km, τ_g = 7000 yr (b) T_e = 20km, τ_g = 5500yr (c) T_e = 40km, τ_g = 5500yr (d) T_e = 40km, τ_g = 3500yr.

https://doi.org/10.5194/se-2021-141
Preprint. Discussion started: 14 December 2021
© Author(s) 2021. CC BY 4.0 License.

Solid Earth Discussions

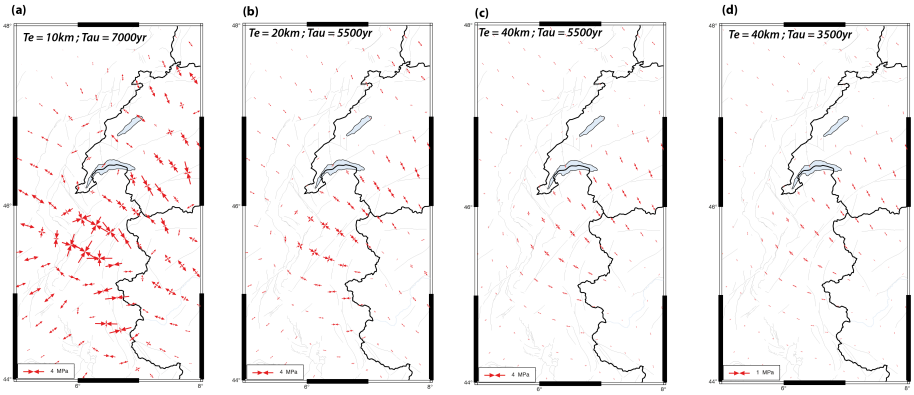

Figure A4. GIA modeled stress fields (a) T_e = 10km, τ_g = 7000 yr (b) T_e = 20km, τ_g = 5500yr (c) T_e = 40km, τ_g = 5500yr (d) T_e = 40km, τ_g = 3500yr.